EUV Full Sun Imaged Spectral Atlas Using the SOHO Coronal Diagnostic Spectrometer

William T. Thompson
SM&A Corporation
Space Sciences Division
9315 Largo Dr. West
Largo, MD 20774
USA

Pål Brekke
ESA Space Science Department
NASA Goddard Space Flight Center
Code 682.3
Greenbelt, MD 20771
USA

(Received ..... ; Accepted in final form .....)

Abstract. The Coronal Diagnostic Spectrometer (CDS) aboard the Solar and Heliospheric Observatory (SOHO) carries out a regular program of measuring the full-disk irradiance using the Normal Incidence Spectrograph (NIS). The full-disk solar spectrum is returned in the wavelength bands 308–379 Å and 513–633 Å, with a spectral resolution between 0.3 and 0.6 Å. A recent modification to the CDS on-board software allows simultaneous moderate resolution monochromatic images to be made of the stronger lines in these wavelength ranges. We report on observations made 23 April 1998, 21 May 1998, and 22 June 1998. A total of 69 monochromatic full-Sun images are extracted from the spectral line data. For the first time, spectrally resolved images of the full Sun in He II 303.8 Å and Si XI 303.3 Å are presented and compared. Velocity maps of the Sun in singly ionized helium are presented. Correlations of intensity to velocity over a wide range of transition region and coronal temperatures are shown. Lines from He I to Fe XIV show statistical redshifts of 1–7 km/s between active regions and quiet Sun areas. Velocity maps of Mg IX and X are presented, showing strong upflow and downflow regions associated with active regions, but not correlated with the brightest emission. Changes in line width are also presented in He I, with discussion of similar features in other lines of comparable temperature. Corrections which need to be applied to CDS/NIS data to extract meaningful velocities and line widths are presented and discussed. The identifications of the lines in the CDS spectrum are examined. The spatial and spectral variation of the background component of the CDS spectrum is examined.

1. Introduction

We report here on a series of observations made of the whole Sun with the Coronal Diagnostic Spectrometer (CDS) aboard the Solar and Heliospheric Observatory (SOHO). These data were primary obtained for monitoring the solar EUV irradiance (Brekke *et al.*, 2000), but also produce monochromatic images of moderate resolution (24×13.3 arc sec) over the complete spectral range from 308–379 Å and 513–633 Å, with sufficient spectral resolution to resolve out individual lines, and to extract Doppler line shifts and line width information. For example, for the first time, spectrally resolved images of the full Sun in the (second order) lines of He II 303.8 Å and Si XI 303.3 Å are presented and compared. Such data are valuable in understanding the relative contribution in broad-band imaging experiments, such as EIT. These data also give a global view of the Sun, and can be used to explore the statistical relationship between intensity and velocity. In addition, they are valuable for checking the identifications of the observed spectral lines.

Prior to SOHO, spatially resolved EUV spectroscopy of the Sun was limited to small regions, or did not return the line shapes. The S082A experiment aboard Skylab (Tousey *et al.*, 1977) used a slitless spectrograph to make high resolution overlapping monochromatic images of the whole Sun. Many spectroscopic observations have been made of subregions, including HRTS (Bartoe and Brueckner, 1975), Skylab S082B (Bartoe *et al.*, 1977), UVSP/SMM (Tandberg-Hanssen *et al.*, 1981), SERTS (Thomas and Neupert, 1994), as well as the CDS and SUMER (Wilhelm *et al.*, 1995) instruments aboard SOHO.

For more than two decades it has been known that UV transition lines show a net redshift on the disk (Doschek, Feldman, and Bohlin, 1976; Brekke, 1993, and references therein; Achour *et al.*, 1995; Brynildsen, Kjeldseth-Moe, and Maltby, 1995). This has been an active area of research for SUMER data (Chae, Yun, and Poland, 1998; Hassler *et al.*, 1999; Teriaca, Banerjee, and Doyle, 1999; Peter and Judge, 1999). Recently, observations of spectrally resolved full-Sun images by the SUMER instrument have been reported on (Wilhelm *et al.*, 1998). Peter (1999a,b) has used this data to explore the velocity properties for chromospheric and transition region lines. Although absolute velocity determinations are not currently possible with CDS data, the present study explores the relationship between relative Doppler shift and solar feature.

2. Observations

The CDS Normal Incidence Spectrometer (NIS) observes the solar spectrum in two wavelength bands between 308–379 Å and 513–633 Å. A grazing incidence Wolter-Schwarzschild type II telescope focuses an image of the Sun onto a slit aperture. The light from the slit illuminates two side-by-side normal incidence toroidal gratings, which then refocus the slit image onto an intensified CCD detector. A scan mirror between the telescope and the slit allows images to be built up by rastering the Sun across the slit. The instantaneous field of view is 4×4 arc min. Movable legs between the instrument and the spacecraft allow the instrument to be pointed anywhere on the Sun. A full description of the instrument can be found in Harrison *et al.* (1995).

The entire solar disk can be observed with CDS by forming a mosaic of 69 individual images (rasters). One such program observes the Sun in six wavelengths to form high-resolution images in small wavelength windows centered on strong lines (Thompson and Carter, 1998). In this observing mode, only the total detector signal in each wavelength band is returned from the spacecraft for each spatial pixel. No line profiles are returned. Such images are monochromatic in that a single line dominates each wavelength window. However, close blends cannot be distinguished. For example, the He II 303.8 Å images also contain a contribution from a nearby Si XI line at 303.3 Å.

Another program which has been used with CDS returns a full-resolution spectral atlas representative of the full-disk irradiance (Brekke *et al.*, 2000). In this program the complete spectrum from both NIS spectral bands are returned from the spacecraft. The spectrum is divided into 1024 pixels each for both wavelength bands between 308–379 Å and 513–633 Å. Instrumental effects limit the spectral resolution to approximately 0.3 and 0.6 Å respectively. The disk is undersampled by a factor of 6—each exposure is taken with a 4×240 arc sec slit, and the individual exposures are separated by 24 arc sec. In the original version of this study, each exposure was summed over the spatial dimension, so that each one-dimensional spectrum returned by the spacecraft represented an area 4×240 arc sec on the Sun. Thus, a full disk irradiance spectrum could be derived from this study, but no solar images.

After the initial runs of this study, a new compression mode was loaded into the CDS onboard software. This new compression mode allows pixels to be binned together in the spatial dimension by a user-selectable binning factor. It was realized that the full-disk irradiance spectrum could be binned onboard by a factor of 8, instead of summing over the entire spatial dimension, with only a small increase in the duration of the study. This allows images of moderate resolution to be returned, as well as the full-resolution irradiance spectrum. Each spatial pixel represents an area of approximately 4×13.3 arc sec on the Sun. Since the scan mirror is moved by 24 arc sec between each exposure, each spatial pixel stands in for an (undersampled) area 24×13.3 arc sec in size. For the remainder of this paper, we will treat the pixel size as 24×13.3 arc sec. Each exposure has a duration of 30 seconds; the full duration of the study is just over 13 hours. We report here on three

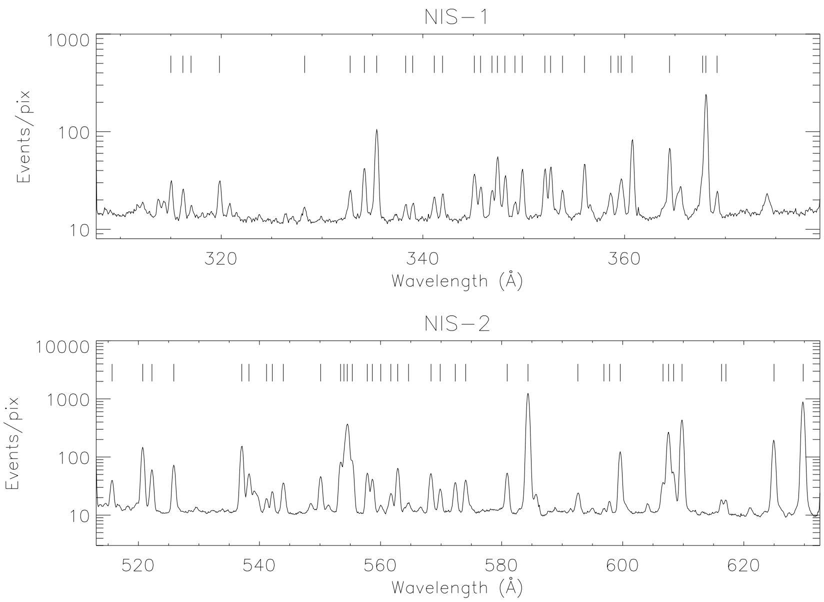

Figure 1. Average full-disk spectrum observed by the CDS Normal Incidence Spectrometer on 23 April 1998. The top plot is of the short wavelength bandpass (NIS-1), and the bottom plot is of the long wavelength bandpass (NIS-2). The data are given in events/pix, for an exposure time of 30 seconds. Spectral lines which are marked have been analyzed to extract monochromatic solar images. See Tables I and II for a complete list of wavelengths and line identifications.

observations made of the full-disk solar irradiance images, on 23 April 1998, 21 May 1998, and 22 June 1998.

3. Line fitting

Figure 1 shows a full-disk irradiance spectrum as observed by CDS on 23 April 1998. The top plot is of the short wavelength bandpass (NIS-1), and the bottom plot is of the long wavelength bandpass (NIS-2). Marked on the figure are those spectral lines whose solar images have been extracted for this study. In the end, 69 wavelengths were selected for analysis. Some spectral lines which were originally considered were later rejected as being too faint for analysis. However, some faint lines were retained to improve the fit of nearby lines. Some lines, particularly in NIS-1, are only valid in the brighter pixels, and do not return a meaningful intensity in low-intensity features such as coronal holes. The final list of lines observed is given in Tables I and II. Wavelengths and line identifications are based on Brooks *et al.* (1999), except for the two Fe XVI lines, which are based on Thomas and Neupert (1994),

Table I. Spectral lines within the NIS-1 band extracted as monochromatic images. Wavelengths are from Brooks *et al.* (1999).

Ion	λ (Å)	Blends
Mg VIII	315.019	
Si VIII	316.215	
Mg VIII	317.028	
Si VIII	319.840	
Al VIII	328.249	
Al X	332.785	
Fe XIV	334.174	
Fe XVI	335.407	Mg VIII 335.231 Å
Fe XII	338.260	
Mg VIII	338.995	
Fe XI	341.152	
Si IX	341.952	
Si IX	345.104	
Fe X	345.716	
Fe XII	346.858	
Si X	347.402	
Fe XIII	348.148	
Mg VI	349.148	(Fe XI 349.046 Å ?)
Si IX	349.856	
Fe XII	352.111	Al VII 352.159 Å, Mg V 352.197 Å
Fe XI	352.671	
Fe XIV	353.793	
Si X	356.037	
Fe XI	358.656	Ne IV 358.7 Å
Ne V	359.374	
Fe XIII	359.777	
Fe XVI	360.798	
Fe XII	364.467	
Mg VII	367.680	
Mg IX	368.059	(Cr XIII/Fe XIII 368.163 Å ?)
Fe XI	369.183	

and the C III line at 574 Å, which is based on Kelly (1987). In cases where multiple lines contributed to the profile, the identification of the line which contributes most to the appearance of the image is given.

Line fitting was performed on data which had been processed through the CDS detector calibration routine VDS_CALIB. This routine applies all known detector effects, including the flat-field response, and a correction for burn-in on the detector. The resulting units are detected photons/pixel/s (referred to in the CDS software as photon-

Table II. Spectral lines within the NIS-2 band extracted as monochromatic images. Wavelengths are taken from Brooks *et al.* (1999), Thomas and Neupert (1994), and Kelly (1987).

Ion	λ (Å)	Blends
He I	515.627	
Si XII	520.685	
He I	522.203	
O III	525.801	Unid.
He I	537.024	
C III	538.299	O II 538.3 Å
Ne IV	541.116	Fe XIV 2×270.522 Å
Ne IV	542.072	
Ne IV	543.881	Si X 2×271.992 Å
Al XI	550.050	
O IV	553.343	
O IV	554.076	
O IV	554.512	
O IV	555.270	
Ca X	557.764	
Ne VI	558.606	Ne VII 558.60 Å
Ne VII	559.985	
Ne VII	561.725	
Ne VI	562.802	Ne VII 562.98 Å
Ne VII	564.568	
Fe XV	2×284.158	Al XI 568.16 Å, Ne V 568.421 Å
Ne V	569.820	
Ne V	572.311	
Ca X	574.052	C III 574.281 Å
Si XI	580.905	
He I	584.340	
Unid.	592.501	
Ca VIII	596.885	
O III	597.823	
O III	599.596	
Si XI	2×303.324	
He II	2×303.784	
O IV	608.312	
Mg X	609.786	O IV 609.829 Å
O II	616.309	
O II	617.034	O IV 617.0 Å
Mg X	624.939	
O V	629.735	

events/pixel/s). The wavelength-dependent response of the instrument was then applied to the fitted intensities. One of the advantages of this approach is that, in detector units, the scattered light background is fairly constant across both NIS wavelength bands.

Gaussian line profiles were fitted within small segments of the spectra containing the desired lines. Depending on the complexity of the spectrum, a segment could contain a single line, or as many as seven lines. The lines in each segment were fitted simultaneously, together with a constant background, using the CFIT program from the CDS software library (available as part of the Solar Software Library at http://sohowww.nascom.nasa.gov/software.html). Line centers were constrained to fit within ± 0.25 Å of the target wavelength, except for the Ne V 359.4 Å and Mg VII 367.7 Å lines which were more tightly constrained (± 0.05 Å) due to their weakness and proximity to the much stronger Fe XIII 359.7 Å and Mg VIII 368.1 Å lines. The main purpose of adding these weaker lines to the analysis was to remove any possible effect they might have on their neighboring lines. Line widths were constrained to be within $\pm 50\%$ of an average full-width-half-maximum (FWHM) value for each line, typically ~ 0.31 Å for NIS-1, and ~ 0.53 Å for NIS-2.

No attempt was made to filter out cosmic ray hits on the detector before making the line fits. It was found that the automated CDS software for recognizing cosmic rays did not perform well on data which had been binned on board the spacecraft. Cosmic rays and other problem pixels can be recognized in the resulting fits in one of several ways:

- The fit fails to converge at a spatial pixel location. These data are flagged by the software.

- The line centroid converges to an extreme value—one of the specified limits of the fit.

- The line width converges to an extreme value.

- The line intensity converges to a conspicuously large value compared to its immediate neighbors. We used the routine CDS_CLEAN_IMAGE from the CDS library against the intensity images to identify the cosmic rays remaining after the previous constraints had been applied.

Figure 2 shows a representative sample of monochromatic images derived from spectral lines ranging in formation temperature from 3×10^4 K to 2.7×10^6 K.

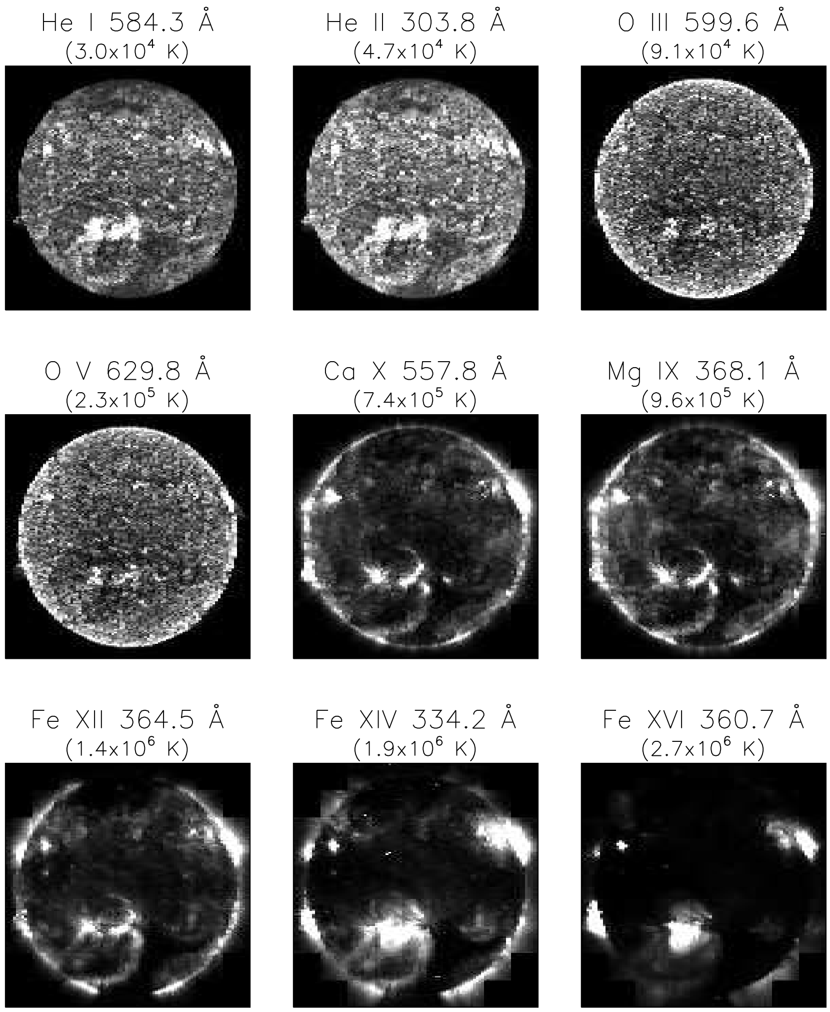

Figure 2. Monochromatic images of a representative sample of spectral lines, ranging in formation temperature from 3×10^4 K to 2.7×10^6 K, taken on 23 April 1998. Although most cosmic rays have been filtered out of the images, using the algorithms outlined in the text, a few cosmic ray hits are still evident in the data.

4. Line identification

As mentioned before, most of the line identifications used come from Brooks *et al.* (1999), hereafter referred to as BROOKS. However, in that work only quiet Sun spectra were observed, and the two Fe XVI lines at 335 and 361 Å do not appear in those data. For those two lines, we depended on the active region spectrum from the 1989 flight of the SERTS sounding rocket (Thomas and Neupert, 1994). Another line which was looked for but not seen in BROOKS, but which was detectable in this work, was the Si X line at 621.11 Å. However, that line was rejected from the final wavelength selection because of its weakness. It is clearly visible, though, in Figure 1.

One of the advantages of these spectrally resolved full-Sun images is that the identification of lines can be easily checked. In BROOKS, position patterns were used to characterize the temperature dependence of lines, and to serve as a check of possible line identifications. In the present work, the images themselves serve that function. When the intensity of a line with a suspected blend is divided by the intensity of an unblended line of the same species, and assuming that the ratio has a density-insensitive ratio, then the blend will show up as excess emission in either quiet Sun or active region/coronal areas, depending on the relative formation temperatures. If the lines being compared have a density-insensitive ratio, then the measured ratio will be unaffected by density variations along the line-of-sight, in the absence of blends. The CHIANTI program (Dere *et al.*, 1997) was used to determine whether the lines being compared should have a density-insensitive ratio. Except where noted, all comparisons below should be unaffected by density.

We found that ratios could be reliably derived down to a peak line intensity of 0.1 events/pix/s. Below this value, the ratio is dominated by random noise. With an exposure time of 30 seconds, this is equivalent to a peak line intensity of 3 events/pix. Folding in typical FWHM line widths of 0.31 Å for NIS-1 and 0.53 Å for NIS-2, this means that one must measure $\gtrsim 15$ events in the line profile for each spatial pixel to get a meaningful peak intensity from the fit.

From line ratio images, we were able to confirm the blends from BROOKS at the following wavelengths: 352.1 Å, 358.6 Å, 541.2 Å, 543.9 Å, 568.3 Å, and 609.8 Å. Using theoretical line ratios generated by the CHIANTI program, we've also been able to confirm the blends at the following wavelengths: 558.6 Å, 562.8 Å, and 617.1 Å. Some identifications are deserving of special notice:

Fe XVI 335.4 Å: This line has long been recognized as being blended in the CDS spectrum with a Mg VIII line at 335.2 Å (Brekke *et al.*, 1997). At low intensity values, the Mg VIII line is a significant contributor to the line profile, and can even dominate the spectrum. In the quiet Sun, the Fe XVI line can disappear completely—it doesn't even appear in the BROOKS quiet Sun spectral atlas. However, from the present data, we find that the Fe XVI line dominates for count rates $\gtrsim 1$ events/pix/s, based on both line centroid position, and comparison with Fe XVI 360.6 Å.

Fe XII 352.1 Å: This line appears to be unblended for count rates $\gtrsim 0.5$ events/pix/s when compared with Fe XII 364.5 Å, but below this rate it is blended with some combination of Al VII and Mg V lines at ~352.2 Å.

Fe XIV 353.8 Å: This line has a potential blend with an Al VII line at the same wavelength. Since Al VII has a significantly lower ionization temperature than Fe XIV, a blend should show up as increased emission in quiet Sun areas. However, comparison of the brightness of the line with Fe XIV 334.2 Å showed no evidence of this. In fact, the appearance of the 353.8 Å line showed a slight amount of increased emission in active regions when compared with the 334.2 Å line. This could be a density effect, as CHIANTI shows that the two Fe XIV lines do not have a density-insensitive ratio.

O III 525.8, 597.8, 599.6 Å: BROOKS lists the O III line at 597.8 Å as having a possible blend with Ca VIII 597.9 Å. Comparison with the O III line at 599.6 Å shows no evidence for such a blend down to 0.1 events/pix/s. However, there does appear to be a small amount of excess emission at 525.8 Å in active regions, particularly in active regions off the limb where it can grow to several events/pix/s.

O IV 553.4, 554.0, 554.5, 555.3 Å: Although the 554.0 Å and 554.5 Å lines have potential blends with second order lines, intensity ratios show that all four lines are unblended.

Ca X 574.0 Å: There are two clues that this line is blended with another, cooler, line. Ratioing the intensity image with the Ca X line at 557.8 Å shows excess emission at 574.0 Å within coronal holes and quiet Sun areas. The plot of intensity versus wavelength also shows a large and unusual redward shift for low intensities, indicating a blend with a cooler line at a wavelength slightly longward of 574.0 Å. Above a count rate of ~2 events/pix/s, the Ca X line seems to dominate. BROOKS does not list any blend for this line; the nearest line listed is an unidentified line at 574.6 Å. We explored whether this line from BROOKS could explain the features we see in Ca X. However, we found that the pixel-by-pixel fitted wavelengths of this blend component showed a strong bimodal distribution, leading to the conclusion that it's better modeled as two components, at roughly 574.3 Å and 574.9 Å respectively. The first of these has a close wavelength coincidence with a C III line at 574.281 Å which is listed in Kelly (1987) as a strong line. Although the line statistics are not sufficient to completely separate the Ca X line from the blend component, it's clear that the blend has relatively stronger emission in quiet Sun and coronal hole areas than Ca X, which is consistent with the identification with C III. The identity of the component at 574.9 Å is unclear.

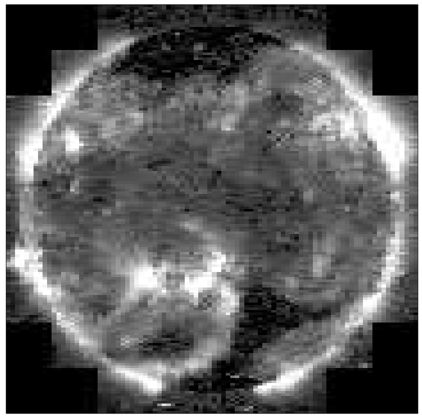

Figure 3. Image formed in the unidentified line at 592.6 Å. Compare with Figure 2. The appearance of the line is consistent with a formation temperature of $\sim 10^6$ K, but cannot be attributed to second-order Si IX.

Unidentified line at 592.6 Å: This line in the CDS spectrum has a possible identification as second order Si IX 296.12 Å. However, this identification was considered in BROOKS and rejected. Those authors also measured a corrected wavelength of 592.501 ± 0.051 Å for this line, which is inconsistent with second-order 296.12 Å. We also are unable to identify this line. The appearance of the line as shown in Figure 3 is consistent with a formation temperature of about 10^6 K, which would favor the identification with Si IX. However, detailed analysis of the ratio of the intensity of this line to other Si IX lines in the spectrum show that they do not match. The 592.6 Å line appears to have a somewhat higher formation temperature than Si IX.

Fe XV 284.2 Å: This second order line is not listed in BROOKS. However, for most of the disk, it appears to be the brightest component which makes up the heavily blended line at this location. The other two components are Al XI 568.2 Å and Ne V 568.4 Å. Based on CHIANTI, the Al XI 568.2 Å component should be 0.489 of the intensity of the Al XI line at 550.0 Å, while the intensity of the Ne V component should be $\sim$0.35 of the intensity of the Ne V line at 569.8 Å. The Fe XV image can then be reconstructed by subtracting the appropriate amounts of Al XI and Ne V. The result of this process is shown in Figure 4. Comparison with an EIT 284 Å image taken during the CDS observation (Figure 11) shows good correspondence except within coronal holes, where the EIT data shows significantly non-zero emission, while the reconstructed CDS data is randomly distributed about zero. This is most likely due to contributions from other lower-temperature lines within the EIT bandpass.

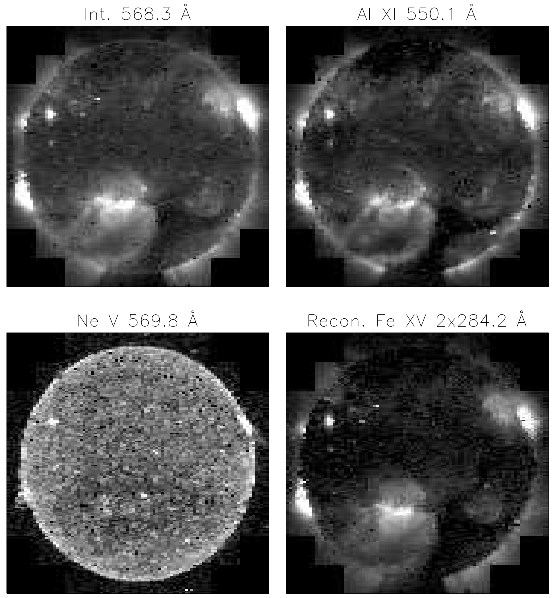

Figure 4. Reconstruction of second-order Fe XV 284.2 Å emission from the measured intensity at 568.3 Å (top-left corner). The contribution from the first order Al XI and Ne V is extrapolated from the measurements at 550.1 and 569.8 Å respectively. The reconstructed Fe XV image is shown in the bottom-right corner.

Mg X 609.8 and 625.0 Å: The Mg X line at 609.8 Å shows a clear excess of emission in quiet Sun and coronal hole areas when compared to Mg X 625.0 Å, confirming the blend with O IV 609.8 Å. There is also the possibility of contamination from a second order Mn XIV, Fe XV blend at 304.9 Å, which is unconfirmed. However, it is not expected to be a significant contributor to the overall intensity at 609.8 Å. The 625.0 Å line also has a potential blend with second-order C IV 312.4 Å. We could find no evidence of this when compared against lines of similar formation temperature (Si IX, Fe XI).

5. He II 303.8 Å and Si XI 303.3 Å

The strongest line in the EUV portion of the solar spectrum is the He II analog of the Ly-α line at 303.8 Å. This is a commonly observed line—for example, on SOHO it is one of the four bandpasses observed by the Extreme Ultraviolet Imager (Delaboudinière *et al.*, 1995), and is the dominant contributor to the full-disk irradiance measurement made by the Solar EUV Monitor on the CELIAS instrument (Hovestadt *et al.*, 1995). Close by to the He II line is a Si XI line at 303.3 Å. All

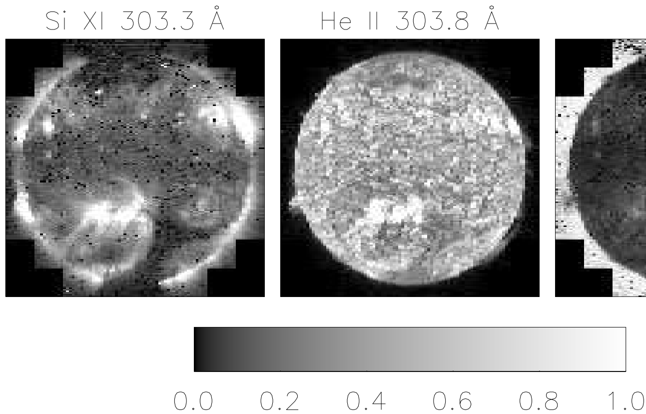

Figure 5. Full-disk images in the closely separated lines Si XI 303.3 Å and He II 303.8 Å for observations made on 23 April 1998. Also shown is the ratio of the Si XI line to the sum of the two lines. The Si XI line is the dominant contributor off the disk. On the disk, He II dominates, but Si XI has a significant contribution near active regions. The color bar along the bottom of the figure shows the mapping of image density to relative intensity and ratio value.

broad-band observations of the He II line will also include a Si XI contribution. It takes a spectrometer to resolve out the contribution of these two closely-spaced lines.

Figure 5 shows images of the Sun in both Si XI 303.3 Å and He II 303.8 Å as seen by CDS on 23 April 1998. Similar images and ratios were also obtained for 21 May 1998 and 22 June 1998. Although the Si XI and He II lines have been separated before (e.g. Thomas and Neupert, 1994), to our knowledge, this is the first time that images of the full disk have been obtained with Si XI separated from He II. Also shown is the ratio of the Si XI line to the sum of the two lines. When this ratio is zero, then all the radiation comes from He II, and when the ratio is 1, then all the radiation comes from Si XI. One can see that Si XI makes up almost all of the radiation off the disk. On the disk and in prominences, the He II line dominates. However, Si XI makes up a significant fraction of the total intensity near active regions. The maximum contribution generally does not occur in the core of the active region, where the He II line is also strong, but in the diffuse area around the core of the active region. There, the He II line is actually

Table III. Typical values of the relative contribution of Si XI 303.3 Å to the total of the Si XI 303.3 Å and He II 303.8 Å lines, as a function of solar feature.

Feature	Relative Contribution
Coronal hole	0.02
Quiet Sun	0.04
Active region core	0.11
Active region diffuse	0.19
Off limb	$\geq$0.90

less intense than in the normal quiet Sun, while the Si XI emission is still enhanced. Typical values for the contribution of Si XI to the intensity around 304 Å are shown in Table III. The off-limb ratio must be considered to be a lower limit, as the He II 303.8 Å component will include a significant contribution from scattered light from the telescope.

6. Velocity images

Since the observations consist of spatially resolved spectra, the Gaussian line fits return not only the peak intensity of the line, but also the wavelength centroids and the line widths (FWHM). In order to convert the wavelengths into velocities, several instrumental effects must first be removed from the data. These are discussed in Appendix B.

6.1. Intensity and velocity correlations

The He II 303.8 Å line shows a weak correlation between the peak line intensity and the centroid wavelength. Active regions will tend to be redshifted compared to the disk median value. This is demonstrated in Figure 6, which shows the He II intensity and velocity images for 21 May 1998. A smoothed version of the velocity map, using a 3×3 boxcar median filter, is also shown to make the correlation more evident. Note in particular the active region belt (marked "A") in the southern hemisphere which is faintly visible in velocity as well as intensity. Figure 7 shows the scatter plot of He II versus velocity. At higher intensities, the velocity distribution is narrower, and biased towards higher (more redshifted) velocities.

The He II 303.8 Å line is not the only line to show statistically significant intensity-velocity correlations. Table IV lists the correlation coefficients for all lines with a statistically significant correlation, where

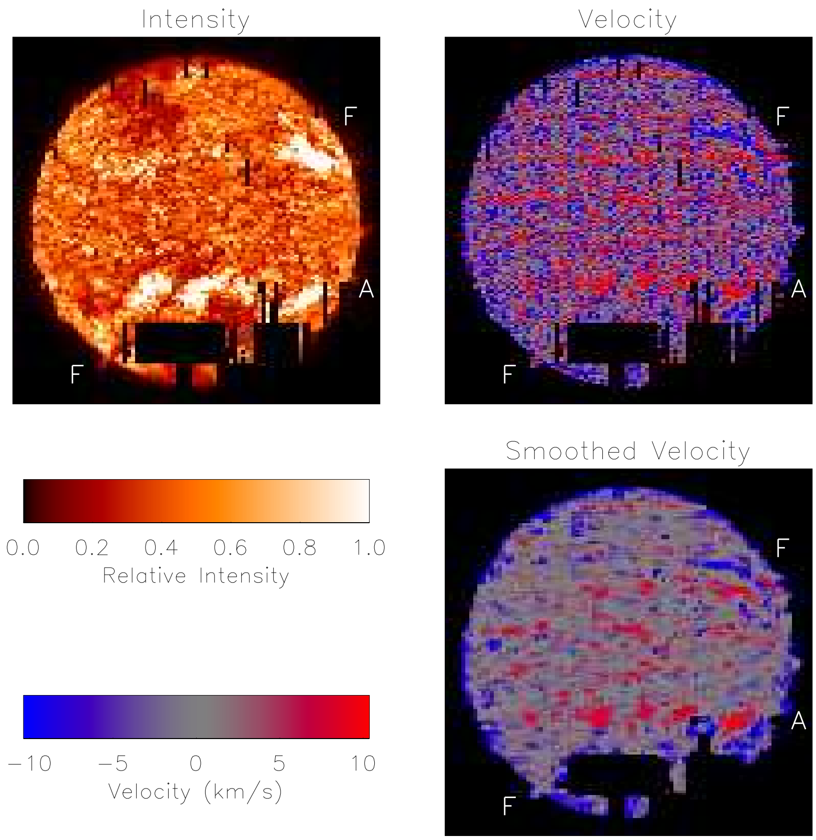

Figure 6. He II 303.8 Å intensity and velocity maps, for 21 May 1998. In the velocity maps, positive values denote shifts towards longer wavelengths (redshifts) and negative values denote shifts towards shorter wavelengths (blueshifts). A smoothed version of the velocity, where a 3×3 boxcar median filter was used, is also shown to highlight the large-scale velocity structures. There is a weak but statistically significant correlation between intensity and velocity, where active regions tend to be redshifted. This can be seen as a slight predominance towards redshift in the southern active region belt, marked by the letter "A". (The westmost active region in that belt is most particularly pronounced in its velocity signature.) There are also strong upflow and downflow regions in the vicinity of filaments. The letters "F" mark two filaments discussed in the text.

the probability of the correlation arising by chance was less than 0.01 for all three datasets. Lines with known blends (see Tables I and II) were excluded. Another criterion for inclusion was that the velocities could be reliably extracted over at least 50% of the image. It was found that for most lines, the peak intensity needed to be at least 0.25 events/pix/s (i.e. $\gtrsim 35$ events) to be able to extract the velocity reliably. Below this

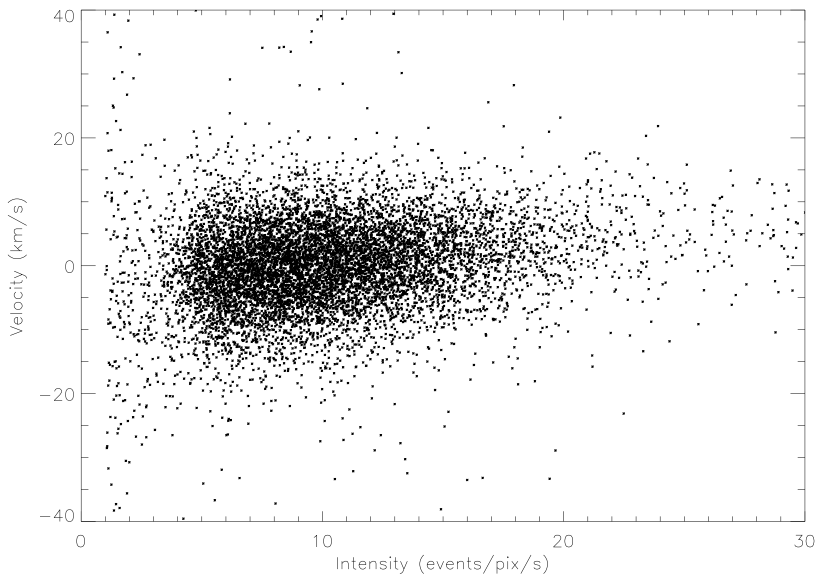

Figure 7. Scatter plot of line intensity versus velocity for the He II 303.8 Å line. A slight shift towards higher velocities (redshift) can be seen for the higher intensity pixels.

value, random noise dominated. A higher threshold was used for a few of the stronger lines.

Note that all but one of the correlation coefficients in Table IV are positive. That is, the wavelength tends to increase (redshift) as the line intensity increases. The single exception is the second-order Si XI 303.3 Å line, which may be affected by its close proximity to the much stronger He II 303.8 Å line. Also shown in Table IV is the shift between the average velocity of the "active" and "quiet Sun" pixels associated with each line. Active pixels are defined as those which are in the top 10% of brightness, while "quiet Sun" pixels are defined as those within ±5% of the median brightness. All but two of the lines show a velocity difference on the order of a few kilometers per second between quiet Sun and active areas. The data for the Ne V line at 569.8 Å is consistent with zero, while the velocity shift of the Si XI line at 303.3 Å is negative, consistent with its negative correlation coefficients. Figure 8 shows the measured velocity difference as a function of formation temperature.

Similar correlations between line intensities and redshifts have been noted by other researchers. Achour *et al.* (1995), using HRTS data, observed differential redshifts between active regions and quiet Sun areas on the order of 2–8 km/s in transition region lines, although little

Table IV. Cross-correlation coefficients between intensity and wavelength (velocity) for each of the three datasets. Only those lines which have statistically significant correlations at the 99% level or better are shown. Lines which are blended (see Tables I and II), and lines for which reliable velocities could be extracted for less than half the pixels, are omitted. Also shown are the associated wavelength shifts Δv, in km/s, between active region and quiet Sun pixels as described in the text. Positive values denote redshift, while negative values denote blueshift. Lines are displayed in approximate order of formation temperature.

		23 April 1998		21 May 1998		22 June 1998	
Ion	λ (Å)	Corr.	Δv	Corr.	Δv	Corr.	Δv
He I	515.7	0.072	3.27	0.086	2.97	0.097	1.50
He I	522.2	0.137	3.80	0.156	3.60	0.159	3.84
He I	537.1	0.158	3.55	0.167	3.16	0.172	3.23
He I	584.4	0.105	1.44	0.098	1.15	0.079	1.03
He II	2×303.8	0.168	3.95	0.182	3.19	0.173	2.96
O III	599.6	0.027	0.27	0.048	0.76	0.038	0.84
O IV	608.4	0.086	1.97	0.096	3.03	0.060	0.45
O V	629.8	0.101	0.97	0.135	0.94	0.116	0.83
Ne V	569.8	0.033	0.74	0.048	-0.78	0.029	-0.20
Mg VIII	315.0	0.063	3.79	0.085	6.65	0.072	6.37
Si VIII	316.2	0.082	4.29	0.131	7.75	0.061	4.67
Si VIII	319.8	0.086	5.36	0.093	4.95	0.093	6.18
Mg IX	368.1	0.051	1.80	0.118	4.24	0.149	4.89
Fe X	345.7	0.069	3.34	0.068	3.81	0.061	4.17
Mg X	625.0	0.044	2.78	0.107	3.64	0.072	3.55
Si IX	349.9	0.061	2.74	0.106	5.40	0.105	4.35
Si X	347.4	0.041	2.85	0.069	3.59	0.067	2.75
Si X	356.0	0.029	1.96	0.053	2.74	0.036	2.18
Fe XII	364.5	0.048	2.67	0.088	4.57	0.090	4.94
Si XI	2×303.3	-0.083	-3.98	-0.062	-4.81	-0.067	-1.74
Si XI	580.9	0.157	7.31	0.166	7.56	0.155	6.68
Fe XIII	348.2	0.163	7.15	0.158	6.35	0.185	9.01
Si XII	520.7	0.080	5.14	0.122	6.20	0.139	7.59
Fe XIV	334.2	0.117	6.61	0.119	6.33	0.145	8.26

or no shift was seen in O V. Differential shifts data as high as 15 km/s were observed by Brynildsen *et al.* (1997) in SUMER data, including O V and Ne VIII. Fredvik and Maltby (1999), using CDS observations of sunspot regions, found large downflows as high as 35 km/s in areas of intense emission for the chromospheric and transition region lines He I 584 Å and O V 630 Å, but no evidence for systematic correlations of downflow with intensity in coronal lines. The advantage of the present observations is that the entire solar disk is sampled, which

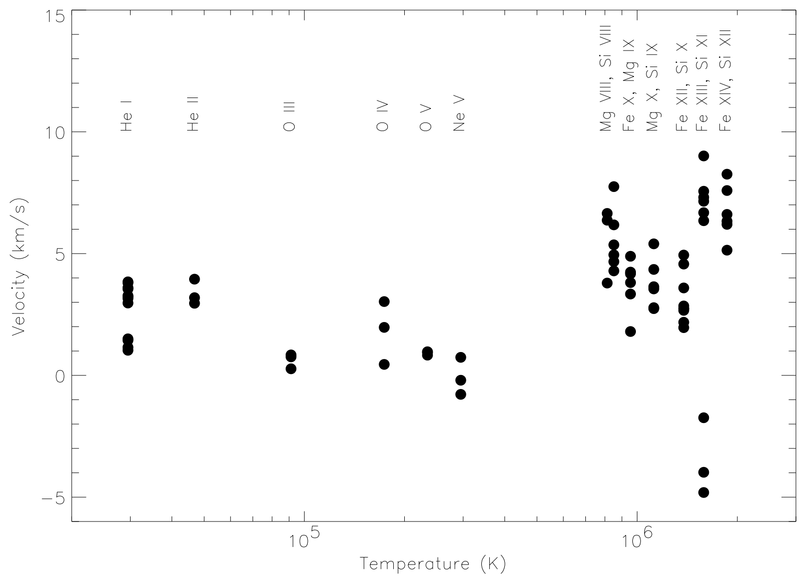

Figure 8. Velocity differences between active and quiet Sun pixels from Table IV as a function of formation temperature. Positive values are redshifts and negative values are blueshifts.

allows the intercomparison of flows over widely separated areas. The case for systematic downflows in Mg IX and X is made in Section 6.3.

Since the data presented here are only moderate resolution, no conclusions can be made about intensity or velocity differences between network cell interiors and boundaries, such as were reported by Hassler *et al.* (1999). As the CDS spatial pixels have been summed onboard in groups of eight, each pixel includes both cell interior and cell boundary emission.

One thing that needs to be considered is whether there are any instrumental effects, or systematic effects in the processing, which could lead to the results in Table IV. There are no known instrumental effects which could systematically shift line center positions as a function of line intensity. Charge transfer efficiency effects in the CCD would act in opposite directions for the NIS-1 and NIS-2 spectra. The He I 584 Å line was used as a velocity reference for the large-scale thermal shifts which needed to be removed from the data. If this line was preferentially blueshifted in the vicinity of active regions, then the derived correction would tend to make the other lines look preferentially redshifted in active regions. However, this is not the case. Table IV and evidence from other researchers (e.g. Fredvik and Maltby, 1999) shows that He I is preferentially redshifted in active regions. If anything, this would imply that the redshift results in Table IV may be underestimated.

Recent evidence shows that lines with formation temperatures above about 5×10^5 K have a net blueshift in the quiet Sun (Peter, 1999a; Peter and Judge, 1999, Teriaca, Banerjee, and Doyle, 1999). The differences between active regions and quiet Sun for the higher temperature lines may be caused by an excess of blueshift in the quiet Sun rather than an excess of redshift in active regions.

6.2. He II 303.8 Å filament velocities

To the upper right of the active region on the northwest limb of the 21 May 1998 image in Figure 6, there are curved narrow regions of strong velocity, both positive and negative, on the order of $\sim$15 km/s. The blueshifted (dark) component is most readily picked out in Figure 6, but there's also a redshifted lane which follows the lower part of the blueshifted lane before veering off towards the limb. These high velocity lanes appear to be associated with a filament channel, although the filament itself is only weakly seen in the higher-resolution EIT 304 Å channel. That may be due in part to contamination from the Si XI 303.3 Å line, since there's a fairly clear indication of a filament in the He II 303.8 A intensity image in Figure 6. (This filament, and another filament discussed below, is marked with an "F" in the intensity image.) This filamentary structure can also be picked out in an Hα image from the Observatoire de Paris in Meudon, although again it's fairly weak. The large filament in the southeast quadrant of the 21 May 1998 image also shows associated positive and negative velocity features. The same filament velocity signatures can also be seen in He I 522.2 Å, 537.1 Å and 584.4 Å. There is also some indication of them in O III 599.6 Å, O IV 555.3 Å, and O V 629.8 Å.

Similar velocity signatures of filaments have been observed before in chromospheric and transition region lines. Redshifts and blueshifts on opposite sides of filaments have been seen by Athay, Jones, and Zirin (1985), Engvold, Tandberg-Hanssen, and Reichmann (1985), Klimchuk (1986), and Magara and Kitai (1999). Athay, Jones, and Zirin (1985) interpret these signatures as evidence of horizontal velocity flows in magnetically sheared regions. Although both red and blueshifts are seen associated with the two filaments in Figure 6, the predominant velocity signature of the two filaments is a blueshift. Blueshifts associated with filaments have been seen by various researchers, including Orrall, Rottman, and Klimchuk (1983), Schmieder *et al.* (1984), Engvold, Tandberg-Hanssen, and Reichmann (1985), and Klimchuk (1986).

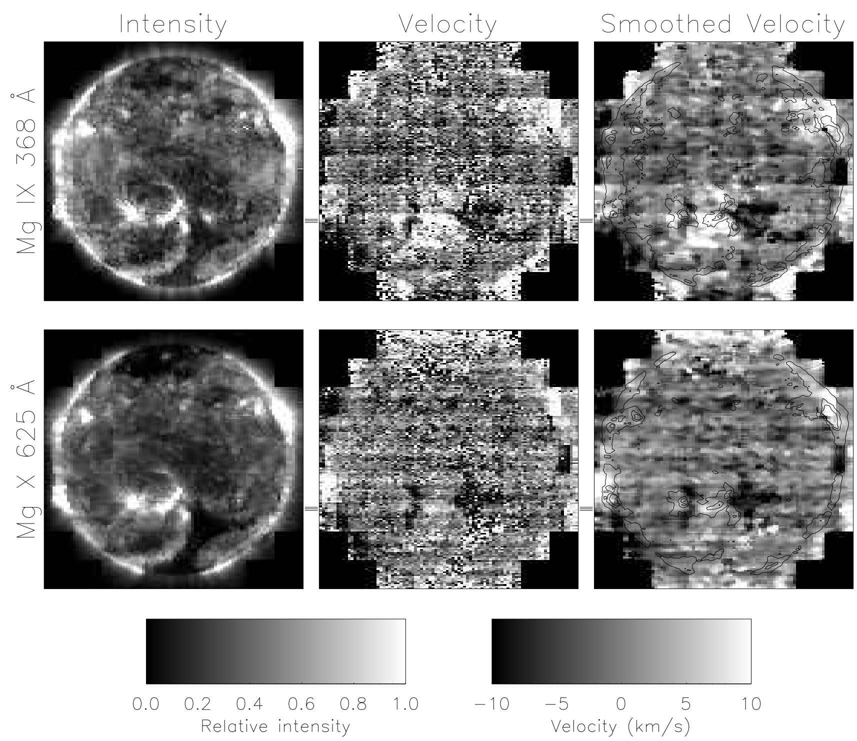

Figure 9. Mg IX 368.1 Å and Mg X 625.1 Å intensity and velocity maps, for 23 April 1998. See Figure 6 for an explanation of the velocity maps. Contours of the intensity images are shown on the smoothed velocity maps for comparison of features. The horizontal bars on the left and right sides of the 23 April velocity image show the location of a trace through the velocity map shown in Figure 10.

6.3. Mg IX 368.1 Å velocities

The single most impressive velocity image is that derived for the Mg IX 368.1 Å line for 23 April 1998 (Figure 9). There is a region of strong downflow (redshift) on the order of 10–15 km/s associated with an active region to the southeast of disk center. This downflow region does not occur in the brightest part of the active region, but in dark regions to the north and south of the bright active region loops, particularly to the south. This region is also dark in other spectral lines, such as He II 303.8 Å, but becomes quite bright in Fe XVI (Figure 2). West of the active region, along the boundary of a northward extension of the south coronal hole, is an area of large upflow. There's also a smaller area of

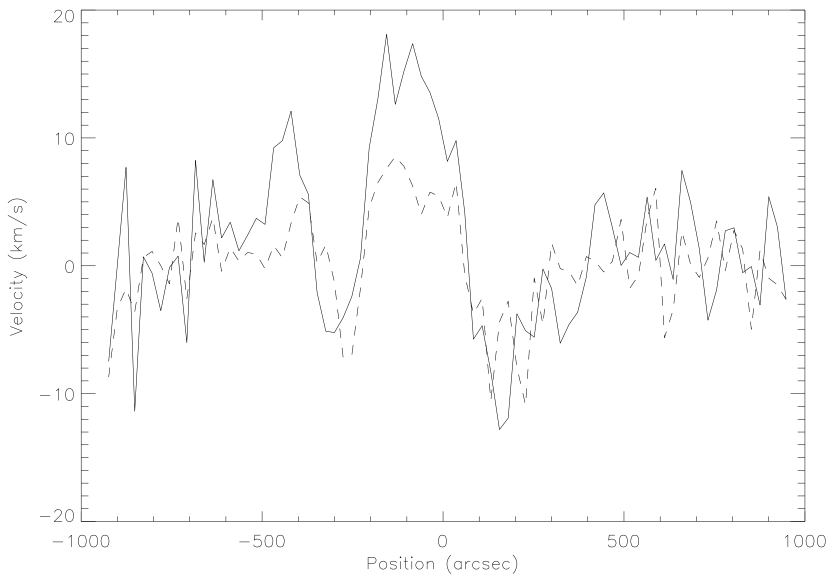

Figure 10. A horizontal trace (solid line) of the Mg IX 368.1 Å velocity map for 23 April 1998, at the location shown in Figure 9. Positive values represent downflows (redshift) and negative values represent upflows (blueshift). Three sequential rows were averaged together to reduce the noise. Also shown (dashed line) is a trace of Mg X 625.1 Å velocities for the same pixels.

strong upflow to the east of the active region. The horizontal bars on the left and right sides of the velocity map in Figure 9 show the location of a horizontal trace of the velocity through these features, which is presented in Figure 10. The velocity maps for the other two dates are not as dramatic as on 23 April. The strongest velocity signatures on those dates appear to be associated with filaments.

The velocity map in Figure 9 is so dramatic compared to other lines in the spectrum that for a while it was assumed to be due to subtle blends with nearby lines. High resolution sounding rocket measurements of the solar spectrum resolved out a weaker component due to a Cr XIII and Fe XIII blend at 368.163 Å (Thomas and Neupert, 1994). However, further analysis has led to the conclusion that the velocity signatures are real. One possible reason that the velocities appear most readily in the Mg IX 368.1 Å line is that it is by far the strongest line in the NIS-1 band over the average Sun, giving good signal-to-noise, and allowing the velocity to be mapped over the entire disk.

Corroborating evidence for the Mg IX velocities shown in Figure 9 can be derived from the Mg X line at 625.0 Å. This is the only other unblended coronal line of comparable brightness to Mg IX 368.1 Å. The

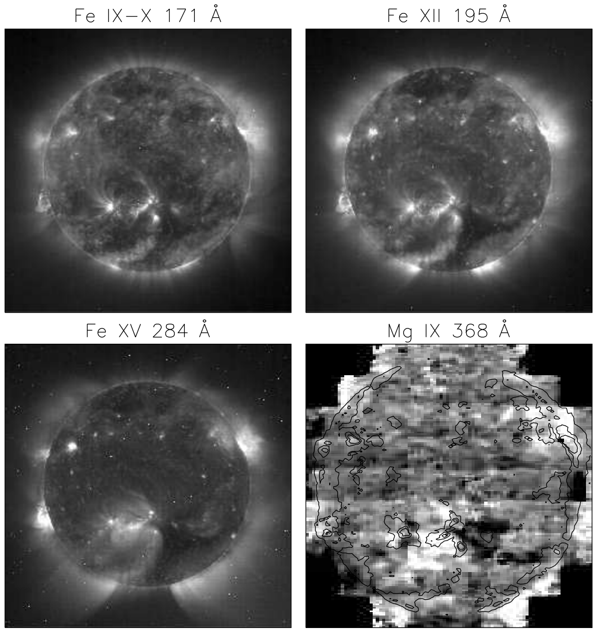

Figure 11. EIT synoptic images in the three coronal bands taken during the CDS full-Sun observations of 23 April 1998. Also shown is the smoothed Mg IX velocity image from Figure 9 for comparison, with the Mg IX intensity contours overplotted.

resulting Mg X velocity images are also shown in Figure 9. Although the amplitudes of the velocities are not the same, the same overall redshifted and blueshifted features appear. The Mg X velocity trace is shown in Figure 10 for comparison with the Mg IX trace over the same pixels. It's possible that an unresolved blend with Cr XIII and Fe XIII at 368.163 Å contributes to the larger redshift seen in Mg IX. The same features are also visible in Si XII 520.7 Å. There's evidence that these features also appear in Si X 347.4 Å and Fe XII 364.5 Å. However, the signal to noise is much poorer in these lines, so the features are much less clear.

Figure 11 shows EIT synoptic images in the three coronal bands taken during the CDS full-Sun observations, together with the Mg IX velocity image from Figure 9. The formation temperature of Mg IX is very similar to that of the EIT 171 Å band, and the images have a very similar appearance. However, the EIT images have much higher resolution, and clearly shows the loop structure of the active region. The region of strong downflows in Mg IX occurs in an area which is relatively dark in Mg IX, but which appears to be associated with large loops as seen in the EIT images, particularly in Fe XV. There is a bright knot of Mg IX emission on the left side of the active region, which appears to be the loop footpoints. The most intense areas of upflow in Mg IX appear to the north and south of this bright footpoint. In MDI data, the bright Mg IX emission occurs in a region of strong positive polarity, and the upflow areas have relatively neutral polarities.

Brown (1996) presents a model in which loops are first quickly heated to 2×10^6 K and filled with material, and then more slowly cool and drain away. The velocity signatures in Mg IX and Mg X may be an indication of that process. The downflows seen in the loop tops may indicate loops in the cooling phase, as the material falls back down, while the upflows seen near the footpoints may be chromospheric evaporation driving the formation of new loops.

Since active regions are shown to have both strong redshift and blueshift features for high temperature lines, and since these features do not have a simple relationship to intensity, care should be taken in interpreting active region velocity data when only a portion of the active region is observed. One can obtain different relationships between intensity and velocity depending on what part of the active region is included in the observations.

7. Line widths

Another product of the Gaussian line fitting technique is the line width. We found that corrections needed to be applied to the line widths for both slit position and scan mirror position, similar to the corrections applied to the line centroid (Section 6). See Appendix B for details.

The measured FWHM line widths appear to be dominated by instrumental effects. During the preflight calibration of CDS, it was determined that the widths of lines on the detector only slightly increased when the slit aperture was changed from 2 arc sec to the 4 arc sec slit used in this study (Bromage *et al.*, 1996; Lang *et al.*, 1999). BROOKS also found no systematic line width variations. Typical widths are $\sim$0.31 Å for NIS-1 and $\sim$0.53 Å for NIS-2. Since expected line widths are on the order of 0.05–0.1 Å (Brosius *et al.*, 1996), CDS is not well suited to measure line widths accurately. When translated into pixels, the FWHM line widths are $\sim$4.5 pixels in both spectral ranges. The 4 arc sec slit used for these data would subtend 2.38 pixels if perfectly imaged.

There are indications of line width variations within the CDS data. In chromospheric and transition region lines, there is an increase in the line width at the limb in coronal holes. This can be seen in Figure 12 which shows the map of the width of the He I 584 Å line, and in Figure 13, which shows vertical and horizontal traces of the line width.

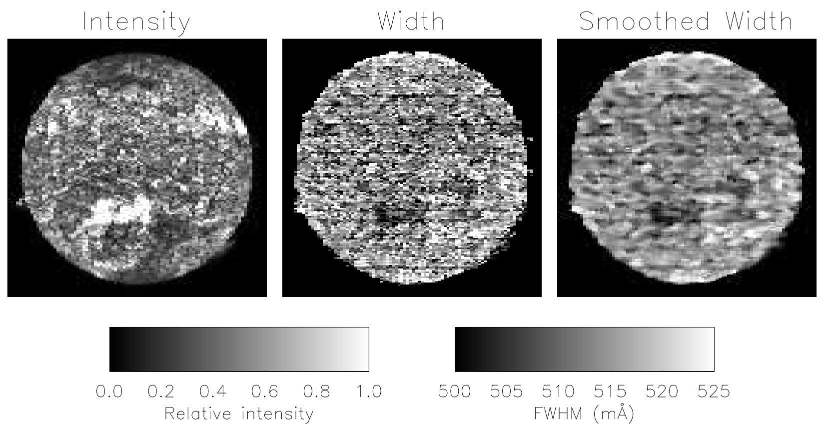

Figure 12. He I 584 Å intensity and line width maps for 23 April 1998. A smoothed version of the line width, where a 3×3 boxcar median filter was used, is also shown to highlight the large-scale width structures. The full range of each width map is from 0.5 Å to 0.525 Å.

The solid line in Figure 13 shows the variation of the line width as one goes from the south pole to the north pole, for the data taken on 23 April 1998. Note that there is a gradual rise in the width as one approaches the south pole, and a sharp increase at the north pole. These features are also seen in He I 522.2 Å and 537.1 Å, He II 303.8 Å, and O V 629.8 Å. This broadening of the He I 584 Å line at the limb in coronal holes was also seen in SUMER data by Peter (1999b), who interprets it as evidence for higher optical depth in coronal holes.

Note also the depression in the line width in the active region around 450 arc sec south of disk center. This is also seen in He I 522.2 Å and O III 599.6 Å. The dashed line shows the variation in the line width as one goes from the east limb to the west limb. There's no evidence of any line width dependence on radial position in the east-west direction. Similar line width features are seen in He I 584 Å from the other two observation dates. Andretta *et al.* (2000) see similar line narrowing in active regions in He II 304 Å. In that work, the broader profiles in the quiet Sun are interpreted as evidence of larger non-thermal velocities, which are presumably suppressed in the higher magnetic fields in active regions.

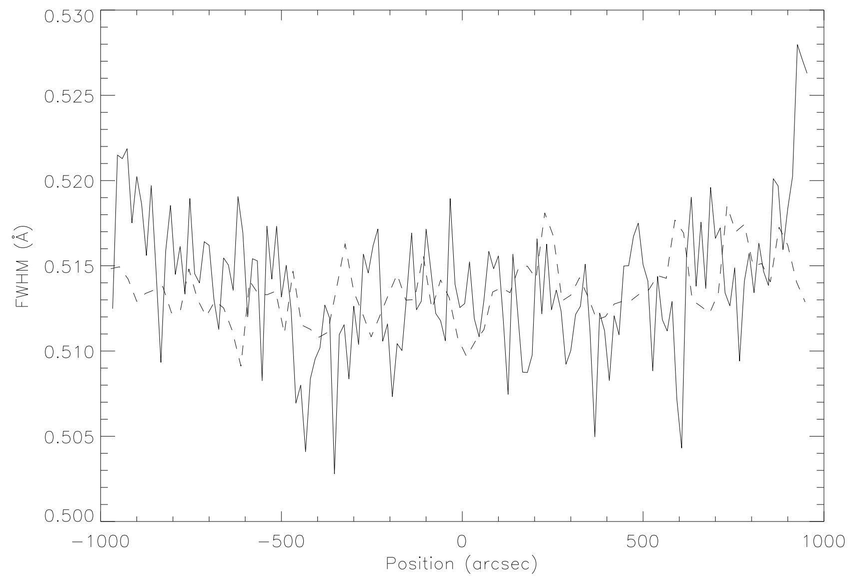

Figure 13. He I 584 Å full-width-half-maximum line width as a function of solar position, for 23 April 1998. The solid line shows the variation of the line width as one goes from the south pole to the north pole, and the dashed line shows the variation in the line width as one goes from the east limb to the west limb. Each curve is based on an average of 20 pixels.

On the other hand, the line width of Mg IX 368 Å is elevated in the region around the active region. Evidence for similar behavior is also seen in Si XII 520.7 Å, but not in Mg X 625.0 Å. The line width is also increased in parts of the corona just above the limb, although not directly over the southern coronal hole. However, because these features are *not* seen in Mg X, we cannot rule out unresolved blends as the source of these features. Of the three parameters describing the Gaussian line profile, the line width is most sensitive to blends.

8. Conclusions

We have demonstrated that the CDS instrument can be used to extract maps of the full Sun in intensity, line shift, and line width. These images can be used to explore the relative contributions of spectral lines to broadband images such as those taken by the Extreme Ultraviolet Explorer. For the first time, spectrally resolved images in the closely separated lines of He II 303.7 Å and Si XI 303.3 Å are presented and compared. We also demonstrate that monochromatic images of the Sun in Fe XV 284 Å can be extracted from CDS data.

Positive correlations of intensity and wavelength are seen in a wide variety of formation temperatures from He I to Fe XIV, with a tendency toward larger redshifts as the intensity increases. The single exception is one of the Si XI lines, which may be affected by the much stronger adjacent He II line. Areas of active Sun have larger redshifts on average than typical quiet Sun regions for all lines except the same Si XI line, and for Ne V which is consistent with zero shift. For temperatures at or above 8×10^5 K, this difference is explained as an excess of blueshift in the quiet Sun.

Mg IX and X velocity maps show features in active regions which can be interpreted as falling material in cooling loops. In areas outside the visible loops, near but not in the footpoints, velocity signatures compatible with chromospheric evaporation can be seen. The large scale of these full-Sun velocity maps bring out features that are difficult to distinguish in the more restricted fields-of-view typically used for spectroscopic observations.

We confirm recent observations of He I line broadening at the limb in coronal holes, consistent with increased optical depth as suggested by Peter (1999b), and of chromospheric line narrowing in active regions. This latter effect has been used by Andretta *et al.* (2000) to demonstrate that there is sufficient microturbulence in the quiet Sun for velocity redistribution to be a significant effect on the brightnesses of Helium emission lines.

The identifications of the lines in the CDS spectrum are examined and compared with earlier work. By intercomparing images of the full Sun, we show which potential blends do affect the data, and which do not. We find that several lines of high formation temperature which are blended in the quiet Sun are not significantly blended in active regions, while the reverse is true for some low temperature lines. An approximate formation temperature of $\sim 10^6$ K is derived for the unidentified line at 592.6 Å. The detection of a previously unreported emission line of C III at 574.281 Å is reported, as well as an unidentified line at 574.9 Å.

Appendix

A. Background images

One of the byproducts of the line fitting process was that it allowed us to explore the properties of the scattered background component. We

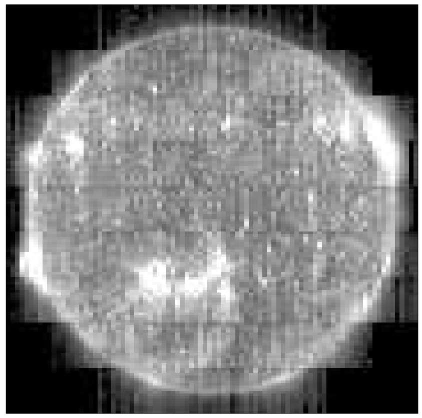

Figure 14. Image formed from the average scattered-light background for the data taken 23 April 1998. This background pattern was found to be consistent over all wavelengths, and in both NIS spectral bands. Compare the above image with Figure 2.

found that the background was spatially resolved, and formed an image of the Sun. (See Figure 14.) The amount of background radiation which needs to be subtracted can vary by more than an order of magnitude from one pixel location to another, tracking the solar features. This behavior is consistent with off-band scattering from the gratings, where light is scattered in the wavelength dispersion direction but not in the spatial direction. Essentially, one is seeing light from the extremely far wings of the grating line profile (e.g. Woods *et al.*, 1994).

Although the amount of background to subtract varies tremendously with spatial position, its dependence on wavelength is very small. Figure 15 shows the background averaged over the entire Sun as a function of wavelength. These data are averaged from the three available datasets on 23 April 1998, 21 May 1998, and 22 June 1998. The wavelength dependence was the same on each of the three dates. The vertical error bars show the 1σ variance at each point, after a small adjustment was made to normalize the three curves to the same average background. One can see that the background level is fairly uniform, showing only small variations with wavelength. (There is a slight correlation with bright spectral lines—note that the background at 584 Å is high compared to its neighbors—but this effect is small compared to the overall amount of background.) This is consistent with the preflight measurements of the amount of light scattered into the CDS bandpass by the flight gratings when exposed to Ly-α radiation (Boucarut *et al.*, 1994). However, the amount of scattered light shown in Figure 15 cannot be explained solely by Ly-α leakage, and the appearance of Figure 14 indicates that the background component must include some

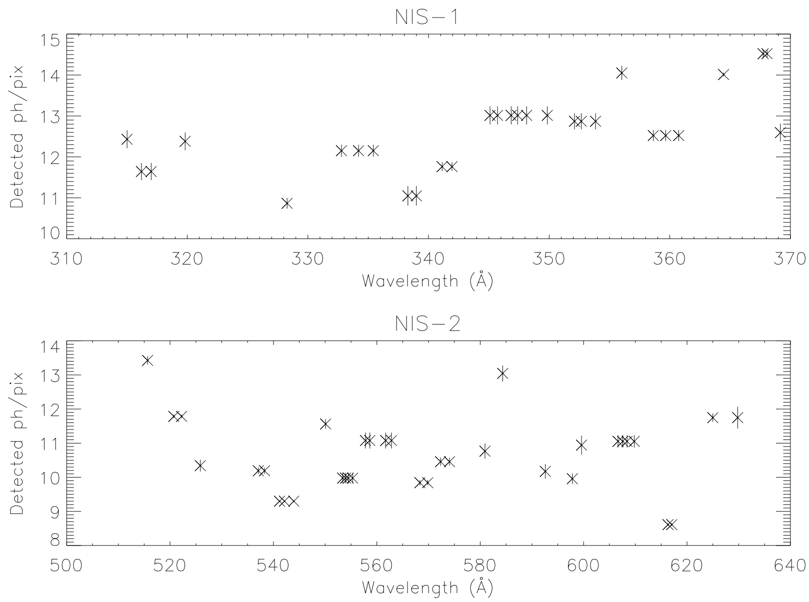

Figure 15. The instrumental scattered light signal, averaged over the solar disk, plotted as a function of wavelength. The top plot is of the short wavelength bandpass (NIS-1), and the bottom plot is of the long wavelength bandpass (NIS-2). The data are given in events/pix, for an exposure time of 30 seconds. Adjacent points with the same value represent lines which were simultaneously fitted.

coronal lines. Most likely the background is formed from a variety of different lines, both shortward and longward of the CDS bandpasses.

B. Velocity and line width corrections

A number of corrections need to be applied to the data to extract meaningful velocities and line widths. Although several of these corrections are now standard in the CDS software, namely the line tilt and scan mirror corrections, to our knowledge they have never before been discussed in print.

Line tilts. The image of the CDS spectrometer aperture slit is not completely vertical on the detector. Instead, it has a slight tilt to it, where the top of the slit appears blueshifted compared to the bottom. The amount of tilt depends on the wavelength. We used the standard tilt correction factors embedded within the CDS software package, namely

$$\begin{aligned} T_1 &= 0.0070771198 - (2.28799 \times 10^{-7})p - (6.36054 \times 10^{-9})p^2 \\ T_2 &= 0.0039751199 + (1.47323 \times 10^{-6})p - (1.266 \times 10^{-8})p^2 + \quad (1) \end{aligned}$$

$$+(1.19576 \times 10^{-11})p^3$$

for NIS-1 and NIS-2 respectively, where, p represents the detector pixel number in the wavelength direction, and T is the tilt in pixels/pixel. For the He II 303.8 Å line, which is seen in second order in NIS-2, we found that we got better results if we used $T = 0.00184$ pixels/pixel. It may be that second-order lines do not follow the same tilt pattern as first-order lines. The same value was also used for Si XI 303.3 Å. (The above numbers refer to detector pixels. Since in the present data, detector pixels were summed together in groups of 8, the above factors had to be correspondingly modified.)

Scan mirror position. The scan mirror between the telescope and the slit changes the illumination pattern on the two NIS gratings. As the scan mirror is moved from one end of its range to the other, there is some tradeoff as to how much of the telescope aperture illuminates the NIS-1 grating, and how much illuminates the NIS-2 grating (Bromage *et al.*, 1996; Lang *et al.*, 1999). This causes a small wavelength shift on the detector. To remove this effect, we adopted the following correction factors:

$$\begin{aligned} \Delta p_1 &= (-0.0030423011)\Delta m - (3.3262600 \times 10^{-5})\Delta m^2 - \\ &\quad -(2.0959131 \times 10^{-7})\Delta m^3 \\ \Delta p_2 &= (-0.0018515786)\Delta m + (2.3390659 \times 10^{-5})\Delta m^2 - \\ &\quad -(4.0578093 \times 10^{-8})\Delta m^3 \end{aligned} \tag{2}$$

for NIS-1 and NIS-2 respectively, where $\Delta m = m - 128$ is the scan mirror position referenced to zero at the center of travel, and Δp is the line shift in pixels to be removed from the line center position. These curves were derived from an analysis of the SOHO daily synoptic images, and are very close to those which were independently derived by S. V. H. Haugan (1998, private communication), and which are now embedded within the CDS software.

Instrument temperature effects. As the image of the solar disk is built up from rastered slit spectra, the thermal environment of the instrument undergoes small variations. This causes small shifts of the spectra on the detector. The effect is minimized with the use of active temperature control of the optical bench. However, a small residual effect remains (e.g. BROOKS). In order to track this effect, we analyzed the behavior of the strong He I 584 Å line. We made the assumption that any large-scale features in the fitted wavelength for this line were due to thermal changes in the instrument. The median shift along the slit was measured for each exposure in the mosaic, and then smoothed within each raster via a five-point boxcar filter. This allows the (presumably instrumental) large-scale features to be tracked without perturbing smaller scale velocity features which are presumed to be solar in nature. The resulting shift in pixels is then applied to the spectrum. All velocities are referenced to the median wavelength for each line over the entire solar image. Therefore, only relative lineshifts can be extracted.

Line width corrections. The corrections adopted for line width were

$$\begin{aligned} \Delta w_1 &= -(3.7151814 \times 10^{-5})\Delta m - (7.6156963 \times 10^{-7})\Delta m^2 + \\ &\quad +(4.4 \times 10^{-5})s \\ \Delta w_2 &= (0.00025243502)\Delta m - (1.5194956 \times 10^{-6})\Delta m^2 + \\ &\quad +(0.000112366)s \end{aligned} \tag{3}$$

for NIS-1 and NIS2 respectively, where s is the position along the slit, from -72 to +72 in detector pixels, $s = 0$ represents the center of the slit, $\Delta m = m - 128$ is the scan mirror position referenced to zero at the center of travel, and Δw is the correction factor to be subtracted from the FWHM width in Ångstroms. It should be noted that the above width corrections are for the 4×240 arc sec slit used in these observations. Different corrections may be needed when the 2×240 arc sec slit is used.

References

Achour, H., Brekke, P., Kjeldseth-Moe, O., and Maltby, P.: 1995, *Astrophys. J.* **453**, 945.

Andretta, V., Jordan, S. D., Brosius, J. W., Davila, J. M., Thomas, R. J., Behring, W., Thompson, W. T., and Garcia, A.: 2000, *Astrophys. J.*, accepted.

Athay, R. G., Jones, H. P., and Zirin, H.: 1985, *Astrophys. J.* **288**, 363.

Bartoe, J.-D. F. and Brueckner, G. E.: 1975, *J. Opt. Soc. Am.* **65**, 13.

Bartoe, J.-D. F., Brueckner, G. E., Purcell, J. D., and Tousey, R.: 1977, *Applied Optics* **16**, 879.

Boucarut, R. A., Leviton, D. B., Thomas, R. J., and Madison, T.: 1994, *SPIE Proc.* **2011**, 565.

Brekke, P.: 1993, *Astrophys. J.* **408**, 735.

Brekke, P., Kjeldseth-Moe, O., Brynildsen, N., Maltby, P., Haugan, S. V. H., Harrison, R. A., Thompson, W. T., and Pike, C. D.: 1997, *Solar Phys.* **170**, 163.

Brekke, P., Thompson, W. T., Woods, T. N., and Eparvier, F. G.: 2000, *Astrophys. J.*, submitted.

Brown, S. F.: 1996, *Astron. Astrophys.* **305**, 649.

Brynildsen, N., Kjeldseth-Moe, O., Maltby, P.: 1995, *Astrophys. J. Lett.* **455**, L81.

Brynildsen, N., Fredvik, T., Maltby, P., Kjeldseth-Moe, O., Brekke, P., Haugan, S. V. H., Harrison, R. A., and Wilhelm, K.: 1997, ESA SP-404, *Proc. of the Fifth SOHO Workshop*, 263.

Bromage, B. J. I., Breeveld, A. A., Kent, B. J., Pike, C. D., and Harrison, R. A.: 1996, University of Central Lancashire Report **CFA/96/09**.

Brooks, D. H., Fischbacher, G. A., Fludra, A., Harrison, R. A., Innes, D. E., Landi, E., Landini, M., Lang, J., Lanzafame, A. C., Loch, S. D., McWhirter, R. W. P., Summers, H. P., and Thompson, W. T.: 1999, *Astron. Astrophys.* **347**, 277-312.

Brosius, J. W., Davila, J. M., Thomas, R. J., and Monsignori-Fossi, B. C.: 1996, *Astrophys. J. Supp.* **106**, 143-164.
Chae, J., Yun H. S., Poland, A. I.: 1998, *Astrophys. J. Supp.* **114**, 151.
Delaboudinière, J.-P., Artzner, G. E., Brunaud, J., Gabriel, A. H., Hochedez, J. F., Millier, F., *et al.*: 1995, *Solar Phys.* **162**, 291.
Dere, K. P., Landi, E., Mason, H. E., Monsignori-Fossi, B. C., and Young, P. R.: 1997, *Astron. Astrophys. Supp.* **125**, 149.
Doschek, G. A., Feldman, U., and Bohlin, J. D.: 1976, *Astrophys. J. Lett.* **205**, L177.
Engvold, O., Tandberg-Hanssen, E., and Reichmann, E.: 1985, *Solar Phys.* **96**, 35.
Fredvik, T. and Maltby, P.: 1999, *Solar Phys.* **184**, 113.
Harrison, R. A., Sawyer, E. C., Carter, M. K., Cruise, A. M., Cutler, R. M., Fludra, A., *et al.*: 1995, *Solar Phys.* **162**, 233.
Hassler, D. M., Dammasch, I. E., Lemaire, P., Brekke, P., Curdt, W., Mason, H., Vial, J.-C., and Wilhelm, K.: 1999, *Science* **283**, 810.
Hovestadt, D., Hilcenbach, M., Bürgi, A., Klecker, B., Laeverenz, P., Scholer, M., *et al.*: 1995, *Solar Phys.* **162**, 441.
Kelly, R. L.: 1987, *J. Phys. Chem. Ref. Data* **16**, Suppl. 1.
Klimchuk, J. A.: 1986, in *Coronal and Prominence Plasma*, ed. A. I. Poland, NASA Conf. Publication 2442, 183.
Lang, J., Kent, B. J., Breeveld, A. A., Breeveld, E. R., Bromage, B. J. I., Hollandt, J., Payne, J., Pike, C. D., and Thompson, W. T.: 1999, Rutherford Appleton Laboratory Technical Report **RAL-TR-1999-036**.
Magara, T. and Reizaburo, K.: 1999, *Astrophys. J.* **524**, 469.
Orrall, F. Q., Rottman, G. J., and Klimchuk, J. A.: 1983, *Astrophys. J. Lett.* **266**, L65.
Peter, H.: 1999a, *Astrophys. J.* **516**, 490.
Peter, H.: 1999b, *Astrophys. J. Lett.* **522**, L77.
Peter, H. and Judge, P. G.: 1999, *Astrophys. J.* **522**, 1148.
Schmieder, B., Malherbe, J. M., Mein, P., and Tandberg-Hanssen, E.: 1984, *Astron. Astrophys.* **136**, 81.
Tandberg-Hanssen, E., Athay, R. G., Beckers, J. M., Brandt, J. C., Bruner, E. C., Chapman, *et al.*: 1981, *Astrophys. J. Lett.* **244**, L127.
Teriaca, L., Banerjee, D., and Doyle, J. G.: 1999, *Astron. Astrophys.* **349**, 636.
Thomas, R. J. and Neupert, W. M.: 1994, *Astrophys. J. Supp.* **91**, 461.
Thompson, W. and Carter, M.: 1998, *Solar Phys.* **178**, 71.
Tousey, R., Bartoe J.-D. F., Brueckner, G. E., Purcell, J. D.: 1977, *Applied Optics* **16**, 870.
Wilhelm, K., Curdt, W. Marsch, E., Schühle, U., Lemaire, P., Gabriel, A., *et al.*: 1995, *Solar Phys.* **162**, 189.
Wilhelm, K., Lemaire, P., Dammasch, I.E., Hollandt, J., Schühle, U., Curdt, W., Kucera, T., Hassler, D.M., and Huber, M.C.E.: 1998, *Astron. Astrophys.* **334**, 685.
Woods, T. N., Wrigley (III), R. T., Rottman, G. J., and Haring, R. E.: 1994, *Applied Optics* **33**, 4273.

Address for correspondence: William T. Thompson
NASA Goddard Space Flight Center
Code 682.3
Building 26, Room G1
Greenbelt, MD 20771
USA